

First-principles study of epitaxial strain in perovskites

Oswaldo Diéguez, Karin M. Rabe, and David Vanderbilt

Department of Physics and Astronomy, Rutgers University, Piscataway, New Jersey 08854-8019, USA

(Dated: November 14, 2018)

Using an extension of a first-principles method developed by King-Smith and Vanderbilt [Phys. Rev. B **49**, 5828 (1994)], we investigate the effects of in-plane epitaxial strain on the ground-state structure and polarization of eight perovskite oxides: BaTiO_3 , SrTiO_3 , CaTiO_3 , KNbO_3 , NaNbO_3 , PbTiO_3 , PbZrO_3 , and BaZrO_3 . In addition, we investigate the effects of a nonzero normal stress. The results are shown to be useful in predicting the structure and polarization of perovskite oxide thin films and superlattices.

PACS numbers: PACS: 77.55.+f, 77.80.Bh, 77.84.Dy, 81.05.Zx

I. INTRODUCTION

Ferroelectrics are insulating solids of technological importance because of their ability to maintain an electric polarization that can be reoriented by the application of an electric field.¹ This property lends itself to technological applications including microelectronic devices and computer memories. Among ferroelectrics, perovskites constitute a subclass that has been of theoretical and experimental interest since the discovery in 1945 of its first member, barium titanate (BaTiO_3). This interest is motivated in part by the relative simplicity of their cubic crystalline phase. For a perovskite of general formula ABO_3 , this structure contains cations A at the cube corners, a cation B at the center of the cube, and oxygen atoms at the center of the cube faces forming a regular octahedron, as depicted in Fig. 1(a). Typically, perovskites are found in this cubic paraelectric phase at high temperature; as the temperature is reduced, symmetry-lowering distortions to other phases, including ferroelectric ones, may occur.

The electronics industry's demands for smaller components have made thin ferroelectric films the subject of recent attention.^{2,3} Experimentally, it is found that the

properties of ferroelectrics in thin-film form generally differ significantly from those in the bulk. While many factors are expected to contribute to these differences, it has been shown that the properties of perovskite thin films are strongly influenced by the magnitude of the epitaxial strain resulting from lattice-matching the film to the substrate, known as misfit strain or epitaxial strain.

Previous theoretical studies have isolated the effects of epitaxial strain on the structure and properties of films by imposing the epitaxial constraint on the in-plane lattice vectors of a periodic bulk sample. Using a phenomenological Landau-Devonshire model, Pertsev, Zembilgotov and Tagantsev⁴ introduced the concept of mapping the equilibrium structure of a ferroelectric perovskite material versus temperature and misfit strain, thus producing a phase diagram of the observable epitaxial phases. Given the importance of strain in determining the properties of these films, these diagrams have proven to be of enormous interest to experimentalists seeking to interpret the results of experiments on epitaxial thin films and heterostructures. This phenomenological approach should give excellent results in the temperature/strain regime in which the model parameters were fitted (usually near the bulk ferroelectric transition) but will generally be less accurate when extrapolated to other regimes. In particular, Figure 1 of Ref. 5 shows that two different sets of parameters can give two quite different phase diagrams. Furthermore, it is only possible to study materials for which all the needed experimental information is available.

In previous work,^{5,6,7} we have examined the effects of epitaxial strain with an analogous, but fully first-principles, approach. Specifically, we presented density-functional theory (DFT)⁸ calculations for the structure and properties of BaTiO_3 , PbTiO_3 and SrTiO_3 with varying in-plane strain, fully relaxing all structural degrees of freedom consistent with uniform distortions (that is, retaining the five-atom unit cell). From this, we obtained zero-temperature phase diagrams that complement the phenomenological results of Pertsev and coworkers. In this paper, we show that these phase diagrams can be reproduced using the first-principles energy parameterization of King-Smith and Vanderbilt, and give results for an additional five perovskite oxides:

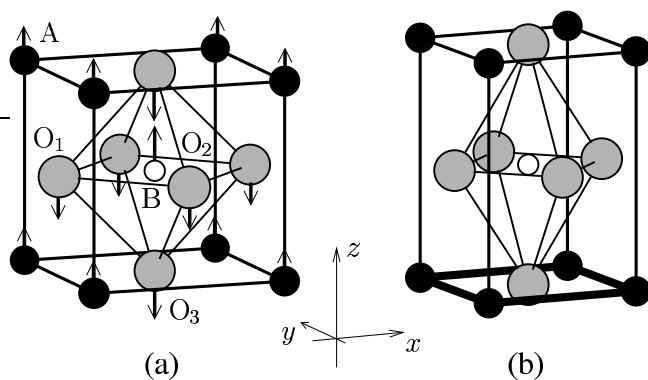


FIG. 1: (a) Ideal cubic perovskite structure for an ABO_3 compound; the z -polarized soft-mode atomic displacements are indicated by arrows. (b) Epitaxial paraelectric (or p) phase, in which the atoms are constrained in the xy plane due to the presence of the substrate.

CaTiO_3 , KNbO_3 , NaNbO_3 , PbZrO_3 , and BaZrO_3 . This approach greatly decreases the computational effort involved in computing the phase diagram and readily allows the inclusion of nonzero external stress.⁹ Moreover, the parameters can be fully specified in a compact table, and the functional form of the energy is suitable for analytical computations and conceptual interpretation, leading to a classification of possible stress-strain phase diagrams. These results can be used for predictions of the structure of epitaxially strained thin films grown on substrates with square symmetry, and for the design of novel perovskite strained-layer superlattices with two or more components.

The paper is organized as follows. In Sec. II we describe the extension of the KSV method to study the effects of the epitaxial strain constraint and external stress, and the first-principles calculations used to obtain the KSV parameters. Section III presents the results for the eight perovskite oxides considered, including the sequence of phase transitions with varying misfit strain at zero stress, and phase diagrams in which we show the most stable phase for given misfit strain and external stress. In Sec. IV, we review the approximations and discuss how to use the present results for the prediction of the structures and polarization of thin films and superlattices. Finally, in Sec. V we present our conclusions.

II. METHOD

A. Formalism

The starting point of this analysis is the parameterized total-energy expression presented by King-Smith and Vanderbilt in Ref. 10. This is a Taylor expansion around the cubic perovskite structure in terms of the six independent components η_i of the strain tensor (i is a Voigt index, $i = 1-6$) and the three Cartesian components u_α ($\alpha = x, y, z$) describing the amplitude of the soft mode defined by the pattern of eigen-displacements associated with the smallest eigenvalue of the (zone-center) force-constant matrix. The arrows in Fig. 1 indicate a typical displacement pattern associated with this mode, greatly magnified to allow its visualization.

The contributions to the energy (per unit cell) can divided into terms arising from pure strain and from pure soft-mode amplitude, and an interaction term,

$$E = E^{\text{elas}}(\{\eta_i\}) + E^{\text{soft}}(\{u_\alpha\}) + E^{\text{int}}(\{\eta_i\}, \{u_\alpha\}), \quad (1)$$

with the zero of the energy corresponding to the cubic structure. For crystals with cubic symmetry the strain energy is given, correct to second order in the strains, by

$$\begin{aligned} E^{\text{elas}}(\{\eta_i\}) = & \frac{1}{2}B_{11}(\eta_1^2 + \eta_2^2 + \eta_3^2) \\ & + B_{12}(\eta_1\eta_2 + \eta_2\eta_3 + \eta_3\eta_1) \\ & + \frac{1}{2}B_{44}(\eta_4^2 + \eta_5^2 + \eta_6^2), \end{aligned} \quad (2)$$

where B_{11} , B_{12} , and B_{44} are related to the elastic constants of the crystal by factors of the cell volume. The soft-mode energy given in Ref. 10 contains terms up to fourth-order in the soft-mode amplitude,

$$E^{\text{soft}}(\{u_\alpha\}) = \kappa u^2 + \alpha u^4 + \gamma(u_x^2 u_y^2 + u_y^2 u_z^2 + u_z^2 u_x^2), \quad (3)$$

where $u^2 = u_x^2 + u_y^2 + u_z^2$, κ is twice the soft-mode eigenvalue, and α and γ are the two independent symmetry-allowed fourth-order coefficients describing the cubic anisotropy. Finally, the interaction between the strains and the soft-mode amplitude is given by

$$\begin{aligned} E^{\text{int}}(\{\eta_i\}, \{u_\alpha\}) = & \frac{1}{2}B_{1xx}(\eta_1 u_x^2 + \eta_2 u_y^2 + \eta_3 u_z^2) \\ & + \frac{1}{2}B_{1yy}[\eta_1(u_y^2 + u_z^2) + \eta_2(u_z^2 + u_x^2) \\ & \quad + \eta_3(u_x^2 + u_y^2)] \\ & + B_{4yz}(\eta_4 u_y u_z + \eta_5 u_z u_x + \eta_6 u_x u_y), \end{aligned} \quad (4)$$

where B_{1xx} , B_{1yy} , and B_{4yz} are the phonon-strain interaction coefficients. All the coefficients in these three parts of the total-energy expression can be obtained from first-principles calculations on a series of distorted structures as described in Ref. 10 and in the next subsection.

In this paper we will be concerned with the effects of strain on a film grown epitaxially on a substrate with square symmetry. The epitaxial strain constraint imposed by the substrate is

$$\eta_1 = \eta_2 = \bar{\eta}, \quad (5)$$

$$\eta_6 = 0, \quad (6)$$

where $\bar{\eta}$ is the misfit strain between the minimum-energy cubic structure of the film material and the substrate.

In the case of epitaxy, where strain elements η_1 , η_2 and η_6 are constrained while the others are not, it is useful to introduce a mixed stress-strain elastic enthalpy $G = E - \sigma_3\eta_3 - \sigma_4\eta_4 - \sigma_5\eta_5$ whose natural variables are u_x , u_y , u_z , η_1 , η_2 , η_6 , σ_3 , σ_4 and σ_5 . Specializing to our case in which $\eta_1 = \eta_2 = \bar{\eta}$, $\eta_6 = 0$, and assuming that the shear stresses σ_4 and σ_5 vanish, we define an effective elastic enthalpy given by

$$\tilde{G} = E - \sigma_3\eta_3 \quad (7)$$

whose natural variables are u_x , u_y , u_z , $\bar{\eta}$ and σ_3 . Using Eqs. (2-4) and minimizing Eq. (7) with respect to η_3 , η_4 and η_5 yields

$$\begin{aligned} \eta_3 = & \frac{1}{B_{11}}[\sigma_3 - 2B_{12}\bar{\eta} \\ & - \frac{1}{2}B_{1xx}u_z^2 - \frac{1}{2}B_{1yy}(u_x^2 + u_y^2)] \end{aligned} \quad (8)$$

$$\eta_4 = -\frac{B_{4yz}}{B_{44}}u_y u_z, \quad (9)$$

$$\eta_5 = -\frac{B_{4yz}}{B_{44}}u_z u_x. \quad (10)$$

Substituting these expressions back into Eq. (7), we express \tilde{G} in terms of its natural variables as

$$\begin{aligned}\tilde{G} = & (A_{\bar{\eta}\bar{\eta}}\bar{\eta}^2 + A_{\bar{\eta}\sigma}\bar{\eta}\sigma + A_{\sigma\sigma}\sigma^2) \\ & + (B_{\bar{\eta}}\bar{\eta} + B_{\sigma\sigma} + B)u_{xy}^2 \\ & + (C_{\bar{\eta}}\bar{\eta} + C_{\sigma\sigma} + C)u_z^2 \\ & + Du_{xy}^4 + Eu_z^4 + Fu_{xy}^2u_z^2 \\ & + Hu_{xy}^4\sin^2\theta\cos^2\theta.\end{aligned}\quad (11)$$

Here we have simplified the notation by replacing σ_3 by σ . Also, the two soft-mode amplitude components are represented in polar coordinates as

$$u_x = u_{xy}\cos\theta, \quad (12)$$

$$u_y = u_{xy}\sin\theta. \quad (13)$$

The coefficients in \tilde{G} are expressed in terms of the KSV parameters as follows:

$$A_{\bar{\eta}\bar{\eta}} = B_{11} + B_{12} - 2\frac{B_{12}^2}{B_{11}}, \quad (14)$$

$$A_{\bar{\eta}\sigma} = 2\frac{B_{12}}{B_{11}}, \quad (15)$$

$$A_{\sigma\sigma} = -\frac{1}{2B_{11}}, \quad (16)$$

$$B_{\bar{\eta}} = \frac{B_{1xx} + B_{1yy}}{2} - \frac{B_{12}}{B_{11}}B_{1yy}, \quad (17)$$

$$B_{\sigma} = \frac{B_{1yy}}{2B_{11}}, \quad (18)$$

$$B = \kappa, \quad (19)$$

$$C_{\bar{\eta}} = B_{1yy} - \frac{B_{12}}{B_{11}}B_{1xx}, \quad (20)$$

$$C_{\sigma} = \frac{B_{1xx}}{2B_{11}}, \quad (21)$$

$$C = \kappa, \quad (22)$$

$$D = \alpha - \frac{1}{8}\frac{B_{1yy}^2}{B_{11}}, \quad (23)$$

$$E = \alpha - \frac{1}{8}\frac{B_{1xx}^2}{B_{11}}, \quad (24)$$

$$F = 2\alpha + \gamma - \frac{1}{4}\frac{B_{1xx}B_{1yy}}{B_{11}} - \frac{B_{1xx}^2}{B_{11}}, \quad (25)$$

$$H = \gamma. \quad (26)$$

For a given set of coefficients in the potential \tilde{G} of Eq. (11), we can predict the phase diagram as a function of misfit strain $\bar{\eta}$ and the normal external stress σ by minimizing \tilde{G} to find the values of the ground-state soft-mode amplitude components. For a fourth order theory, like the present KSV expression, the entire optimization process can be done analytically, since it is possible to compute first and second derivatives of \tilde{G} and to do a stability analysis of the various possible phases, classified by the nature of the minimum-energy soft-mode vector. For example, a paraelectric p phase similar to the cubic

TABLE I: Summary of epitaxial perovskite phases. Columns list, respectively, the phase, space group, and symmetry of the soft-mode amplitude components.

Phase	SG	SMA components
p	$P4mmm$	$u_x = u_y = u_z = 0$
c	$P4mm$	$u_x = u_y = 0, u_z \neq 0$
a	$Pmm2$	$u_x \neq 0, u_y = u_z = 0$
aa	$Amm2$	$u_x = u_y \neq 0, u_z = 0$
ac	Pm	$u_x \neq 0, u_y = 0, u_z \neq 0$
r	Cm	$u_x = u_y \neq 0, u_z \neq 0$

phase can appear if the potential is minimized for $\mathbf{u} = 0$, but relaxation along \hat{z} will occur, making the cell tetragonal, as shown in Fig 1(b). The classification, following Pertsev and coworkers,⁴ is given in table I. Expressions for the elastic enthalpy of a given phase as a function of misfit strain can be obtained by minimizing Eq. (11) with the appropriate constraint on \mathbf{u} . For example, the elastic enthalpies for the p , c , a and aa phases are

$$\tilde{G}_p = A_{\bar{\eta}\bar{\eta}}\bar{\eta}^2 + A_{\bar{\eta}\sigma}\bar{\eta}\sigma + A_{\sigma\sigma}\sigma^2, \quad (27)$$

$$\tilde{G}_c = \tilde{G}_p - \frac{(C + C_{\bar{\eta}}\bar{\eta} + C_{\sigma}\sigma)^2}{4E}, \quad (28)$$

$$\tilde{G}_a = \tilde{G}_p - \frac{(B + B_{\bar{\eta}}\bar{\eta} + B_{\sigma}\sigma)^2}{4D}, \quad (29)$$

$$\tilde{G}_{aa} = \tilde{G}_p - \frac{(B + B_{\bar{\eta}}\bar{\eta} + B_{\sigma}\sigma)^2}{4D + H}. \quad (30)$$

The process of generating the stress-strain diagrams is thus extremely rapid in comparison with a full DFT analysis, once the KSV parameters have been obtained from first principles calculations as described in the next section. Justification of the approximations involved has been presented in Ref. 10, and will be discussed further in Sec. IV.

B. First-principles calculations of the coefficients

In Table V of their paper,¹⁰ King-Smith and Vanderbilt report the computed coefficients to be used in their model. We have now repeated calculations analogous to theirs, taking advantage of the increase in computational power that has taken place during the last ten years to push the boundaries of the numerical approximations that control the accuracy of the first-principles calculations. We used the same local-density approximation^{11,12} DFT methodology and the same ultrasoft pseudopotentials that they used.¹³ In our case, the plane-wave kinetic-energy cutoff has been raised to 50 Ry, and the Monkhorst-Pack¹⁴ k-point mesh is finer, containing $8 \times 8 \times 8$ points.

The lattice parameters and the soft-mode eigenvector components calculated for the eight perovskites under study are reported in Table II. These values are quite similar to those reported in Tables IV and VII of Ref. 10,

TABLE II: Lattice parameters (in bohr) and soft-mode eigenvector components (normalized to unity) for eight perovskites, calculated using DFT.

	a_0	ξ_A	ξ_B	$\xi_{O_{1,2}}$	ξ_{O_3}
BaTiO ₃	7.448	0.184	0.774	-0.218	-0.522
SrTiO ₃	7.285	0.490	0.596	-0.408	-0.270
CaTiO ₃	7.201	0.678	0.363	-0.435	-0.171
KNbO ₃	7.470	0.195	0.796	-0.325	-0.341
NaNbO ₃	7.395	0.427	0.638	-0.428	-0.209
PbTiO ₃	7.337	0.597	0.487	-0.411	-0.262
PbZrO ₃	7.762	0.769	0.152	-0.438	-0.044
BaZrO ₃	7.846	0.703	0.275	-0.462	-0.054

where a comparison with experimental and other theoretical data can also be found.

Following the prescription given by King-Smith and Vanderbilt,¹⁰ we found the updated KSV parameters displayed in Table III. The two final columns of this table contain the values of α' and γ' , the coupling constants whose values determine the symmetry of the low-temperature phase for bulk perovskites¹⁵ (see Ref. 10). Most of the parameters are only slightly different from those given in Table V of Ref. 10, and we have found that the predictions that both sets give for the epitaxial films are qualitatively the same (note, however, that cubic SrTiO₃ changes from being marginally unstable to marginally stable). The differences are mainly related to the use of finer grids in our case when performing the fast Fourier transforms required in the calculations. On the other hand, the improvements in plane-wave cutoff and k -point mesh have a quite small impact on the values of the coefficients.

For our discussion of the effects of epitaxial strain on the polarization, it is useful to have an expansion not just of the energy, but also of the polarization, in terms of the soft-mode amplitude. The linearized expression

$$P_z = \frac{e}{\Omega} z^* u_z \quad (31)$$

is adequate for most purposes. Here e is the absolute value of the electron charge, Ω is the unit cell volume of the perovskite, and z^* is the Born effective charge of the soft mode, given in terms of the soft-mode eigenvectors of Table II by

$$z^* = Z_A^* \xi_A + Z_B^* \xi_B + 2Z_{O_{1,2}}^* \xi_{O_{1,2}} + Z_{O_3}^* \xi_{O_3}. \quad (32)$$

We take the Born effective charges Z^* for each atom to have their values in the cubic structure as calculated by Zhong, King-Smith, and Vanderbilt.¹⁶ Using these together with the eigenvectors reported in Table II we obtain the following values for z^* : 9.94 (BaTiO₃), 8.65 (SrTiO₃), 7.03 (CaTiO₃), 11.06 (KNbO₃), 9.14 (NaNbO₃), 9.40 (PbTiO₃), 6.29 (PbZrO₃), and 5.69 (BaZrO₃). This approximate expression neglects the possible dependence of the Born effective charges upon the strain.

III. RESULTS

A. Calculations at zero external stress

We first consider the case in which the external perpendicular stress σ vanishes. Table IV shows the sequence of transitions that occurs for each of the eight perovskites studied as the misfit strain increases, and the values of strain at which the transitions occur.

The observed sequences of phases can be understood with the help of Fig. 2, which illustrates the types of elastic enthalpy behaviors that we observe for the materials considered. At the strains at which a transition occurs from one phase to another, the energy curves join smoothly, indicating that these transitions are of second order. It can be shown analytically that this is indeed the case for the KSV model, and that at the symmetry-breaking transitions ($c-r$, $aa-r$, $a-ac$, $p-c$, $p-a$, or $p-aa$) the higher-symmetry phase becomes unstable. For all compounds considered, we see that for sufficiently high compressive strains, the lowest energy phase is always the c phase, in which the atomic displacements and therefore the polarization point in the [001] direction, perpendicular to the substrate. On the other hand, for sufficiently high tensile strains, we obtain a phase in which the polarization lies in the substrate plane, pointing along [100] (a phase) for BaZrO₃ or along [110] (aa phase) for the rest of the compounds. The in-plane orientation is determined by the sign of H (i.e., of γ), which is positive for BaZrO₃ and negative for the seven other compounds. In the intermediate strain regime, three different behaviors are found. For BaTiO₃, KNbO₃, NaNbO₃, and PbZrO₃, an r phase appears between the c and aa phases, as in Fig. 2(a). The fact that these perovskites crystallize in the r phase at low absolute values of strain is not surprising, since this phase is the most similar to the rhombohedral phase that they adopt as the bulk ground state according to the KSV theory (see Table VI of Ref. 10). For SrTiO₃ and BaZrO₃ it is the paraelectric p phase that appears at intermediate strains, as in Fig. 2(b). For these two compounds, no r or ac phase appears. Instead, the polarization along [001] continuously goes to zero as the strain becomes less compressive, and only reappears in the xy plane once the tensile strain reaches some given value, continuously growing from then on. The epitaxial paraelectric p phase is the analog of the bulk cubic phase (see Fig. 1(b)), which is the ground state predicted by the KSV theory with the parameters of Table III for both bulk SrTiO₃ and bulk BaZrO₃. Finally, for CaTiO₃ and PbTiO₃ yet another behavior is obtained, as shown in Fig. 2(c). At intermediate strains, the rhombohedral phase is the lowest energy single phase. However, partly because of its inverted-parabola elastic enthalpy curve, the common tangent line between the c and aa phases yields a lower energy in the intermediate strain regime, and thus a mixed phase of c and aa domains is expected.

The strain-induced phase transitions found using this approach compare well with the full DFT results previ-

TABLE III: Coefficients of energy expansion, Eqs. (1-4), for eight perovskites, in atomic units. Coefficients α' and γ' are not directly relevant for this work, but are included for completeness (see Ref. 10).

	B_{11}	B_{12}	B_{44}	B_{1xx}	B_{1yy}	B_{4yz}	κ	α	γ	α'	γ'
BaTiO_3	4.62	1.80	1.79	-2.21	-0.19	-0.10	-0.0143	0.347	-0.488	0.192	-0.129
SrTiO_3	4.97	1.50	1.54	-1.28	0.06	-0.12	0.0010	0.124	-0.161	0.074	-0.036
CaTiO_3	5.34	1.24	1.41	-0.65	0.09	-0.11	-0.0070	0.031	-0.017	0.019	0.012
KNbO_3	6.66	1.03	1.46	-2.91	0.37	-0.03	-0.0155	0.439	-0.655	0.257	-0.178
NaNbO_3	6.15	1.18	0.98	-1.71	0.51	-0.02	-0.0130	0.209	-0.298	0.124	-0.050
PbTiO_3	4.58	1.86	1.40	-0.79	-0.05	-0.07	-0.0117	0.052	-0.020	0.031	0.029
PbZrO_3	5.34	1.64	0.93	-0.20	0.06	0.01	-0.0185	0.013	-0.013	0.011	-0.008
BaZrO_3	5.69	1.46	1.45	-0.44	0.05	-0.12	0.0087	0.013	0.003	0.008	0.012

TABLE IV: The sequence of epitaxially-induced phase transitions and the values of strain $\bar{\eta}_\perp$ and $\bar{\eta}_\parallel$ at the boundary of the c phase and of the aa (or a) phase, respectively. An asterisk denotes the strain regime where formation of mixed domains of c and aa phases could be favorable.

	Sequence	$\bar{\eta}_\perp (10^{-3})$	$\bar{\eta}_\parallel (10^{-3})$
BaTiO_3	$c-r-aa$	-5.89	7.59
SrTiO_3	$c-p-aa$	-2.24	1.59
CaTiO_3	$c-*-aa$	-2.30	5.35
KNbO_3	$c-r-aa$	-4.80	5.49
NaNbO_3	$c-r-aa$	-5.52	4.13
PbTiO_3	$c-*-aa$	-3.00	8.42
PbZrO_3	$c-r-aa$	-52.06	30.42
BaZrO_3	$c-p-a$	-53.41	41.86

ously reported for BaTiO_3 ,⁵ PbTiO_3 ,⁶ and SrTiO_3 .⁷ We look now in detail at this comparison for BaTiO_3 . Figure 3 shows the energy curves of the various phases as predicted by the KSV theory (right panel), to be compared with the full DFT results (left panel). The agreement between the two sets of results is very good, with the small differences present arising from two sources. First, the first-principles calculations in Ref. 5 were performed using the projector-augmented wave method,¹⁷ while the first-principles calculations used to obtain the KSV coefficients in the present work were performed using ultrasoft pseudopotentials.¹³ Second, there are the intrinsic errors due to the use of a Taylor expansion described in the previous section, which are expected to grow as the strain and soft mode magnitudes increase.

Figure 4 shows the displacements of the atoms from their centrosymmetric perovskite positions as strain varies. Again, the agreement of the KSV results (right panel) with the full DFT results (left panel) is very good. In particular, the square root behavior predicted by the KSV theory is exhibited by the more exact DFT calculations. As the in-plane strain increases, we observe a second-order phase transition ($c-r$), and while the magnitude of the atomic displacements continues to diminish along [001], the displacements in the xy plane begin to grow. With increasing tensile strain, the displacements along [001] vanish at the $r-aa$ transition, while the dis-

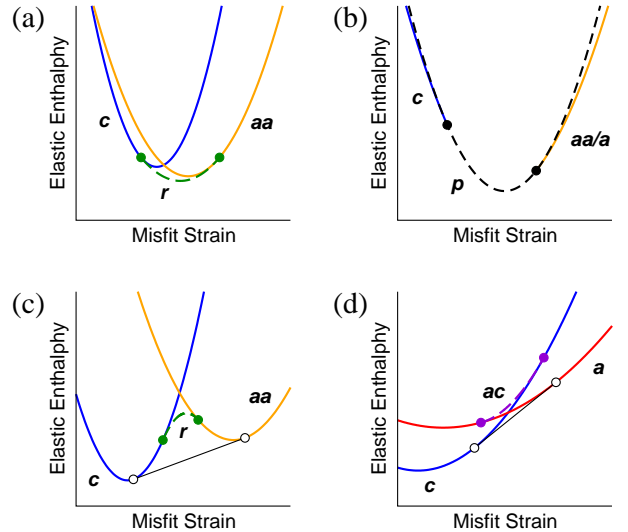


FIG. 2: Sketches of different behaviors found for the elastic enthalpy curves of the most stable phases. Solid circles show where two parabolas meet. Empty circles show the points where a tie line meets a parabola. The curves that meet at the circles do so with equal first derivatives.

placements in the xy plane continue to grow smoothly. In this way, we see that the polarization vector continuously rotates in going from the c phase through the r phase to the aa phase. A quantitative limitation of using a single misfit-strain-independent local mode in the KSV model is shown here in the form of an artificial constraint equating the $\Delta_y(O_1)$ and $\Delta_x(O_3)$ displacements. This constraint is removed when full DFT calculations are performed and the atoms are free to relax within the given space group, but the magnitude of these displacements is not very different from that obtained in the KSV theory.

Figure 5 shows the values of P_z for the various compounds as a function of misfit strain. The square-root singularity at $P_z=0$ corresponds to an $r-aa$ or $c-p$ transition. The slope discontinuity visible at finite P_z in some curves corresponds to the $c-r$ transition of Fig. 2(a), while the termination of the curves at finite P_z for CaTiO_3 and PbTiO_3 corresponds to the encounter with the tie line in Fig. 2(b). The general trend, of course, is a

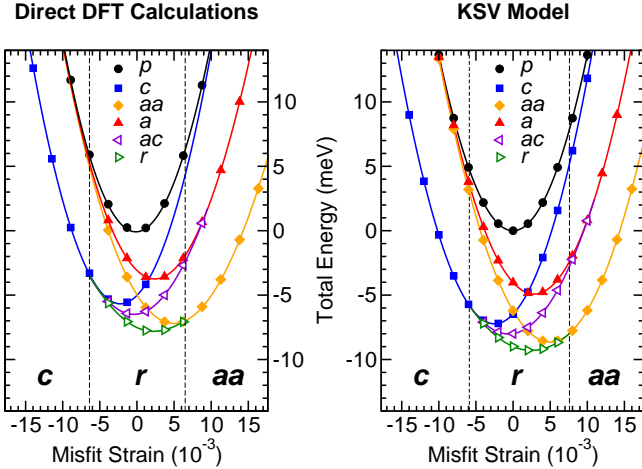


FIG. 3: Comparison of BaTiO₃ energy curves for the six epitaxial phases studied, as obtained from direct DFT calculations⁵ (left), and from the KSV theory (right). Energies are relative to the paraelectric structure at zero misfit strain. The lines in the left panel and the symbols in the right panel are provided as guides to the eye.

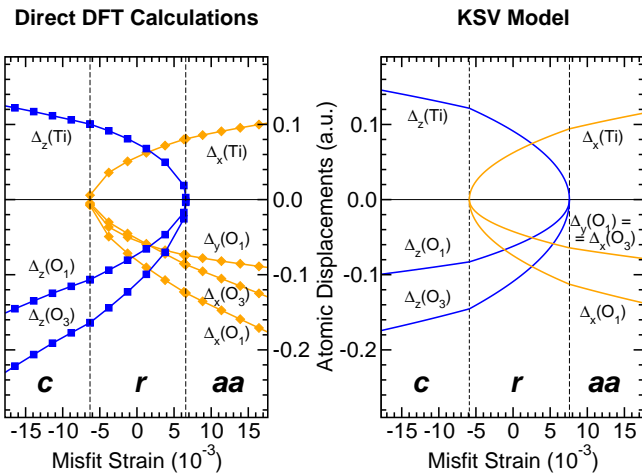


FIG. 4: Comparison of BaTiO₃ atomic displacements for the most stable phase at each given value of strain, as obtained from direct DFT calculations⁵ (left), and from our KSV model (right). $\Delta_z(\text{Ti})$ indicates the displacement of the Ti atom along the z direction, etc. Symmetry implies that $\Delta_y(\text{Ti}) = \Delta_x(\text{Ti})$, $\Delta_x(\text{O}_2) = \Delta_y(\text{O}_1)$, $\Delta_y(\text{O}_2) = \Delta_x(\text{O}_1)$, $\Delta_z(\text{O}_2) = \Delta_z(\text{O}_1)$, and $\Delta_y(\text{O}_3) = \Delta_x(\text{O}_3)$. The lines in the left panel are guides to the eye.

strong increase of P_z with compressive strain, with considerable enhancement possible over the zero misfit strain value. Interestingly, according to this plot CaTiO₃ would have a large P_z if the zone boundary distortions that are present in its actual ground-state crystal structure were suppressed. This result is supported by recent full DFT calculations.¹⁸

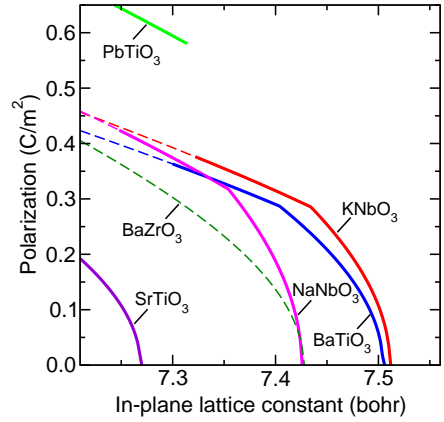


FIG. 5: Value of the polarization along the z axis for different perovskites. The continuous thick part of each curve indicates easily achievable misfit strain conditions, with misfit strain values between -20×10^{-3} and 20×10^{-3} , while the thin dashed part of each curve corresponds to larger strains. The curves for CaTiO₃ and PbZrO₃ fall outside the plotted region.

B. Stress-strain phase diagrams

We now consider application of a nonzero normal stress σ . The stress-strain phase diagrams obtained for each of the eight perovskites are shown in Fig. 6.

All eight diagrams show a universal topology with straight-line phase boundaries meeting at a single crossing point. The perfect linearity of the boundaries is an artifact of the truncation of our energy expansion to fourth order, but the presence of a single crossing point is robust against the introduction of small higher-order terms. The crossing point strain $\bar{\eta}_x$ and stress σ_x can be connected with the critical strain and stress in the isotropic cubic perovskite at which a structural instability first occurs as the pressure is reduced or made more negative. There are two main variants of the diagrams in Fig. 6, the first with four phases (c , r , p , and aa/a), and the second with three phases (c , p , aa/a and a mixed phase region). The varied behavior of the zero-stress diagrams of Fig. 2 can now be interpreted, in the context of Fig. 6, as reflecting whether the zero-stress axis lies above, or below, σ_x .

More specifically, the coordinates of the crossing point can be expressed as functions of the total-energy coefficients as follows:

$$\bar{\eta}_x = \frac{B_\sigma C - BC_\sigma}{B_{\bar{\eta}} C_\sigma - B_\sigma C_{\bar{\eta}}} = -\frac{2\kappa}{B_{1xx} + 2B_{1yy}}, \quad (33)$$

$$\sigma_x = \frac{BC_{\bar{\eta}} - B_{\bar{\eta}} C}{B_{\bar{\eta}} C_\sigma - B_\sigma C_{\bar{\eta}}} = \bar{\eta}_x (B_{11} + 2B_{12}). \quad (34)$$

The strain and stress values at the crossing point are rather modest, with the single exception of PbZrO₃. PbZrO₃ has the lowest soft-mode eigenvalue, and therefore the most negative value of κ (Table III). Its x -polarized soft-mode eigenvalue also changes more slowly on application of an η_1 strain, resulting in a less negative

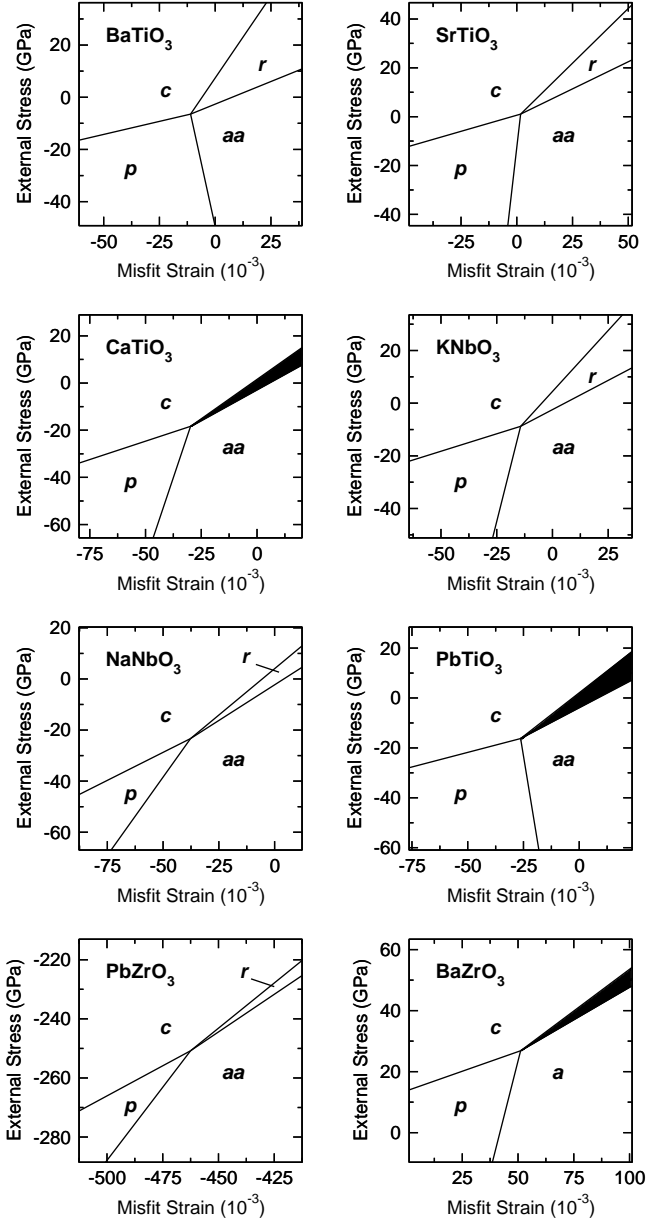


FIG. 6: External stress versus misfit strain phase diagrams for eight epitaxially strained perovskites. Straight lines represent second-order phase transitions. Shadowed areas indicate the presence of *c* and *aa* (or *a*) domains.

value of B_{1xx} . These values of κ and B_{1xx} result in $\bar{\eta}_x$ and σ_x being about an order of magnitude more negative for PbZrO_3 than for the other seven compounds.

For external stresses below σ_x , the behavior is similar in all eight compounds, showing a *c-p-aa* (*c-p-a* for BaZrO_3) sequence of second-order phase transitions, with the elastic enthalpies of the phases behaving as in Fig. 2(b). In this fourth-order KSV theory, the phase

boundaries are straight lines given by

$$\sigma_{c-p} = -\frac{C}{C_\sigma} - \frac{C_{\bar{\eta}}}{C_\sigma} \bar{\eta}, \quad (35)$$

$$\sigma_{p-aa} = -\frac{B}{B_\sigma} - \frac{B_{\bar{\eta}}}{B_\sigma} \bar{\eta}. \quad (36)$$

Rewriting these expressions as functions of the fundamental coefficients of Table III, we see that the value of B_{1yy} plays a central role. For materials like the ones we are studying, for which $B_{11} > 0$, $B_{12} > 0$, and $B_{1xx} < 0$, the slope of the *c-p* transition line is found to be positive if

$$\frac{B_{12}}{B_{11}} > \frac{B_{1yy}}{B_{1xx}}. \quad (37)$$

For all eight perovskites this slope is indeed positive, since the left hand side of the inequality is positive, and B_{1yy} is positive or only slightly negative but much smaller in magnitude than B_{1xx} (the latter being the case for BaTiO_3 and PbTiO_3). The slope of the *p-aa* transition is positive if

$$\frac{B_{12}}{B_{11}} > \frac{1}{2} \left(1 + \frac{B_{1xx}}{B_{1yy}} \right), \quad (38)$$

where the inequality is not satisfied for BaTiO_3 and PbTiO_3 , which have negative values for B_{1yy} . Therefore, for these two perovskites a transition from the *aa* to the paraelectric *p* phase is induced by applying a sufficiently high external tensile stress at fixed misfit strain, while for the others the transition would be from the *p* to the *aa* (or *a*, in the case of BaZrO_3) phase.

For external stresses above σ_x , two kinds of behaviors are found. Five of the perovskites (BaTiO_3 , SrTiO_3 , KNbO_3 , NaNbO_3 , and PbZrO_3) show a *c-r-aa* sequence of second-order phase transitions under these conditions, with the energies of the phases behaving as in Fig. 2(a). In this case, the phase boundaries are straight lines of the form

$$\sigma_{c-r} = -\frac{2BE - CF}{2B_\sigma E - C_\sigma F} - \frac{2B_{\bar{\eta}}E - C_{\bar{\eta}}F}{2B_\sigma E - C_\sigma F} \bar{\eta}, \quad (39)$$

$$\sigma_{r-aa} = -\frac{2C(D + H/4) - BF}{2C_\sigma(D + H/4) - B_\sigma F} - \frac{2C_{\bar{\eta}}(D + H/4) - B_{\bar{\eta}}F}{2C_\sigma(D + H/4) - B_\sigma F} \bar{\eta}. \quad (40)$$

For all five compounds, the slopes of both boundaries are positive.

The other behavior observed for external stress above σ_x is one in which *c* and *aa* (or *a*, in the case of BaZrO_3) domains are expected. The energy curves behave either as shown in Fig. 2(c) (for CaTiO_3 and PbTiO_3) or as shown in Fig. 2(d) (for BaZrO_3). However, in the intermediate region, instead of a uniform phase, the system is expected to break into domains, as explained in the previous section for PbTiO_3 and CaTiO_3 at zero external stress.

IV. DISCUSSION

In this section, we first consider in detail the several approximations that are responsible for the ease and simplicity with which we can generate stress-strain phase diagrams for perovskites. We then discuss and give examples of the applicability of the theory to realistic experimental studies of perovskite films and superlattices.

Within the KSV theory the thermodynamical potential is expanded as a Taylor series in strain and soft-mode amplitude, where the reference used is the perfect cubic perovskite of Fig. 1(a). The truncation at low order in the variables of the expansion means that the expansion decreases in accuracy for large distortions. As relevant misfit strains are generally rather small (less than 2%), this appears not to have significant implications. In addition, in the present form of the theory, the modes selected for the expansion allow only phases that involve five-atom unit cells to be considered. In particular, we do not take into account the possibility of cell-doubling oxygen octahedra rotations, which have been shown to be important in SrTiO_3 ,^{19,20} CaTiO_3 ,²⁰ and PbZrO_3 .²¹ In principle, such rotations could condense in the other compounds under high enough misfit strains, but for BaTiO_3 it has been shown⁵ that this does not occur until one reaches experimentally irrelevant strains, and we expect that this will also be the case for most of these other compounds. Second, our calculations are done at zero temperature. Extending them to finite temperatures could in principle be done using an effective Hamiltonian method as we did in Ref. 5 for BaTiO_3 . However, this would involve designing for each perovskite an effective Hamiltonian along the lines described by Zhong, Vanderbilt, and Rabe,²² and is left for future work. Third, our model does not include the small effect of the zero-point motion of the ions (see Ref. 23 for a discussion). Finally, our theory relies on the LDA to compute the exchange and correlation terms in DFT. This introduces small systematic errors in the calculation, the most important of which is probably the error in the equilibrium lattice constant. However, such errors are well understood and well characterized in perovskites, and tend to be similar for different materials of this class, so that there is a tendency for cancellation of errors in relative quantities such as misfit strains (see, for example, Ref. 10).

The phenomenological Landau-Devonshire approach⁴ also requires approximations, which we review here for the purposes of comparison. Its starting thermodynamical potential is the bulk free energy expanded in polarization and stress, with linear temperature dependence in selected coefficients. Sixth order terms are needed as their importance increases at finite temperature.²⁴ The reference used is the paraelectric cubic perovskite phase at the bulk critical temperature T_c , and the parameters are fit to reproduce experimental observations of the behavior near the bulk ferroelectric transition. For the epitaxial strain dependence, a Legendre transformation is then made to obtain the potential as a function of po-

larization and misfit strain. With parameters extrapolated to zero temperature, this can be compared to the potential in the present work using the linear relation between the polarization and the soft mode amplitude (31). Due to the way in which the parameters are fit, the Landau-Devonshire potential will give its most accurate results for small misfit strains and temperatures near the bulk T_c , while the first-principles potential will be more reliable for the zero-temperature misfit-strain phase diagram.

We now turn to the applicability of our theory to the prediction and understanding of properties of experimentally relevant systems. We first discuss the case of thin films, and then consider the case of strained-layer superlattices.

The theory presented here can be used directly to predict the structure and polarization of a single-domain perovskite-oxide thin film grown on a substrate with square-lattice symmetry. The effects of epitaxial strain will be most evident in films coherent with the substrate. In equilibrium, coherent epitaxial growth is possible up to a certain critical thickness, which depends upon the misfit between film and substrate materials as well as upon temperature and other growth conditions. Using low-temperature synthesis, coherence can be maintained far beyond the equilibrium critical thickness, as has been shown for BaTiO_3 grown on GdScO_3 (−1.0% misfit strain).²⁸ Under such coherent conditions, the full misfit should be used as the input for our theory. For example, in the case of BaTiO_3 on GdScO_3 , Fig. 6 shows a predicted enhancement of P_z from 0.21 to 0.31 C/m² as a result of a 1.0% reduction of the in-plane lattice constant from the theoretical ground-state value of 7.448 bohr to 7.374 bohr. For thicker, partially-relaxed films, the strain should be taken to correspond to the in-plane lattice constant measured for the film²⁹; this assumes that all the misfit dislocations responsible for the relaxation are located at the interface. These predictions are based on the assumption that the epitaxial strain strongly dominates other factors in determining the state of the film.

Similarly, for strained-layer superlattices, the structure and polarization of a perovskite-oxide layer in a superlattice will in general be significantly different from the corresponding bulk. The states of the component layers will largely be determined by the in-plane strain imposed by lattice matching to the other components and/or to the substrate, and can be obtained by referring to the theoretical phase diagrams at the relevant value of misfit strain. In addition, the normal component of the polarization in each layer, at the common in-plane strain, is an important consideration in determining the structure and polarization of the overall superlattice. If the normal polarization is discontinuous, electrostatic energy considerations will tend to polarize the low-polarization layer and depolarize the high-polarization layer to make the normal polarization uniform through the sublattice,²⁵ with accompanying changes in the normal strain of the layer. As an example, this analysis

has proved useful in the interpretation of first-principles results and experiments on the structure of partially-relaxed $\text{SrTiO}_3/\text{BaTiO}_3$ superlattices.^{26,27}

First-principles information about the effects of epitaxial strain on the structure and polarization of component layers also allows us to determine the relative stability of a given superlattice. It is well known that lattice matching of the components minimizes the elastic energy and thus increases the stability. In the case where one or more components have a nonzero normal polarization, the electrostatic energy of the superlattice can be minimized by “polarization matching,” where the components are selected to have the same normal polarization at the common in-plane strain. For example, according to our calculations, BaTiO_3 and NaNbO_3 have the same normal polarization of 0.34 C/m^2 at a common in-plane theoretical lattice constant of 7.336 bohr , corresponding to small compressive misfit strains of less than 0.2% , and thus this is a favorable combination with respect both to elastic and electrostatic energy. In general, however, it is not possible to minimize both elastic and electrostatic energy in this way, and a trade-off between the two is necessary to form the superlattice.

It should be kept in mind, however, that for both films and superlattices, the assumptions that the system is in a single domain and that the epitaxial strain strongly dominates other factors will not be valid in all cases. Phase diagrams including multiple-domain states have, for example, been discussed in Refs. 29,30,31. Other influences that may be important include surface relaxation and reconstruction, atomic and electronic rearrangements at the interface, imperfectly compensated macroscopic elec-

tric fields, deviations from stoichiometry, and the presence of defects.

V. SUMMARY

We have applied the first-principles total-energy parameterization of King-Smith and Vanderbilt¹⁰ to study the effects of epitaxial strain and external stress on the structure and properties of perovskites. We report phase diagrams and polarizations for the same set of eight compounds as in Ref. 10: BaTiO_3 , SrTiO_3 , CaTiO_3 , KNbO_3 , NaNbO_3 , PbTiO_3 , PbZrO_3 , and BaZrO_3 . An updated set of parameters, computed with a comparable first-principles method at higher precision, are provided in Table III. The simple form of the parameterization is seen to be useful in reducing the computational effort for generating these phase diagrams relative to full first-principles calculations, and many features of the phase diagrams can be extracted and interpreted analytically.

We have discussed the use of these results in predicting the structure and polarization of epitaxial perovskite films and strained layer superlattices. Additional properties of interest, such as dielectric or piezoelectric constants can also be computed within this framework.

Acknowledgments

We thank Javier Junquera for useful discussions. This work was supported by ONR Grants N0014-05-1-0054, N00014-00-1-0261, and N00014-01-1-0365, and DOE Grant DE-FG02-01ER45937.

¹ M. E. Lines and A. M. Glass, *Principles and Applications of Ferroelectrics and Related Materials* (Clarendon Press, Oxford, 1977).

² C. H. Ahn, K. M. Rabe, and J.-M. Triscone, *Science* **303**, 488 (2004).

³ M. Dawber, K. M. Rabe, and J. F. Scott, cond-mat/0503372.

⁴ N. A. Pertsev, A. G. Zembilgotov, and A. K. Tagantsev, *Phys. Rev. Lett.* **80**, 1988 (1998).

⁵ O. Diéguez, S. Tinte, A. Antons, C. Bungaro, J. B. Neaton, K. M. Rabe, and D. Vanderbilt, *Phys. Rev. B* **69**, 212101 (2004).

⁶ C. Bungaro and K. M. Rabe, *Phys. Rev. B* **69**, 184101 (2004).

⁷ A. Antons, J. B. Neaton, K. M. Rabe, and D. Vanderbilt, *Phys. Rev. B* **71**, 024102 (2005).

⁸ P. Hohenberg and W. Kohn, *Phys. Rev.* **136**, B864 (1964).

⁹ A. Y. Emelyanov, N. A. Pertsev, and A. L. Khoklin, *Phys. Rev. B* **66**, 214108 (2002).

¹⁰ R. D. King-Smith and D. Vanderbilt, *Phys. Rev. B* **49**, 5828 (1994).

¹¹ W. Kohn and L. J. Sham, *Phys. Rev.* **140**, A1133 (1965).

¹² D. M. Ceperley and B. J. Alder, *Phys. Rev. Lett.* **45**, 566 (1980).

¹³ D. Vanderbilt, *Phys. Rev. B* **41**, 7892 (1990).

¹⁴ H. J. Monkhorst and J. D. Pack, *Phys. Rev. B* **13**, 5188 (1976).

¹⁵ The last column in Table V of Ref. 10 contains values that are not consistent with equation (19b) of the paper. The correct values are: -0.147 (BaTiO_3), -0.051 (SrTiO_3), 0.017 (CaTiO_3), -0.113 (KNbO_3), -0.041 (NaNbO_3), 0.014 (PbTiO_3), -0.008 (PbZrO_3), and 0.014 (BaZrO_3). Since the sign of γ' for each perovskite has not changed, the conclusions concerning phase transitions given in their paper still hold.

¹⁶ W. Zhong, R. D. King-Smith, and D. Vanderbilt, *Phys. Rev. Lett.* **72**, 3618 (1994).

¹⁷ P. E. Blöchl, *Phys. Rev. B* **50**, 17953 (1994).

¹⁸ S. Nakhmanson, K. M. Rabe and D. Vanderbilt, cond-mat/0505491.

¹⁹ W. Zhong and D. Vanderbilt, *Phys. Rev. B* **53**, 5047 (1996).

²⁰ D. Vanderbilt and W. Zhong, *Ferroelectrics* **206-207**, 181 (1998).

²¹ D. J. Singh, *Ferroelectrics* **194**, 299 (1997).

²² W. Zhong, D. Vanderbilt, and K. M. Rabe, *Phys. Rev. Lett.* **73**, 1861 (1994); W. Zhong, D. Vanderbilt, and K. M. Rabe, *Phys. Rev. B* **52**, 6301 (1995).

²³ J. Íñiguez and D. Vanderbilt, Phys. Rev. Lett. **89**, 115503 (2002).

²⁴ J. Íñiguez, S. Ivantchev, J. M. Perez-Mato, and A. García Phys. Rev. B **63**, 144103 (2001)

²⁵ J. B. Neaton and K. M. Rabe, Appl. Phys. Lett. **70**, 321 (2003).

²⁶ K. Johnston and K. M. Rabe, Phys. Rev. B **71**, 100103 (2005).

²⁷ S. Rios, A. Ruediger, A. Q. Jiang, J. F. Scott, H. Lu and Z. Chen, J. Phys: Condens. Matter **15**, L305 (2003).

²⁸ K. J. Choi, M. Biegalski, Y. L. Li, A. Sharan, J. Schubert, R. Uecker, P. Reiche, Y. B. Chen, X. Q. Pan, V. Gopalan, L.-Q. Chen, D. G. Schlom, and C. B. Eom, Science **306**, 1005 (2004).

²⁹ J. S. Speck and W. Pompe, J. Appl. Phys. **76**, 766 (1994).

³⁰ N. A. Pertsev and V. G. Koukhar, Phys. Rev. Lett. **84**, 3722 (2000).

³¹ Y. L. Li, S. Choudhury, Z. K. Liu and L. Q. Chen, Appl. Phys. Lett. **83**, 1608 (2003).